



# Ni–B amorphous alloy nanoparticles modified nanoporous Cu toward ethanol oxidation in alkaline medium



Shu-Jin Zhang <sup>a</sup>, Yi-Xiong Zheng <sup>a,\*</sup>, Lin-Shan Yuan <sup>a</sup>, Li-Hua Zhao <sup>b</sup>

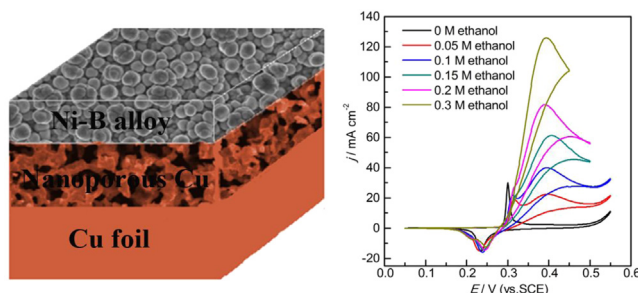
<sup>a</sup> College of Material Science and Engineering, Huaqiao University, Xiamen 361021, PR China

<sup>b</sup> College of Materials, Xiamen University, Xiamen 361005, PR China

## HIGHLIGHTS

- Highly dispersed Ni–B amorphous alloy catalyst supported on NPC is prepared.
- Lower onset oxidation potential of ethanol at Ni–B/NPC than bulk Ni electrode.
- Superior activity for ethanol oxidation at Ni–B/NPC electrode.
- Superior stability for ethanol oxidation at Ni–B/NPC electrode.

## GRAPHICAL ABSTRACT



## ARTICLE INFO

### Article history:

Received 23 May 2013

Received in revised form

13 August 2013

Accepted 30 August 2013

Available online 8 September 2013

### Keywords:

Dealloying

Nanoporous copper

Ultrasonic-assisted electroless

Nickel–boron amorphous alloy

Ethanol

Electrocatalytic oxidation

## ABSTRACT

Nanoporous Cu (NPC) prepared by dealloying CuZn alloy is used as an economic substrate for the fabrication of Ni–B alloy (Ni–B/NPC) by ultrasonic-assisted electroless technique. The results of scanning electron microscopy (SEM) and X-ray diffraction (XRD) demonstrate the NPC has a bicontinuous network structure and the Ni–B/NPC alloy is amorphous structure with highly dispersed nanoparticles. Electrochemical performances are measured by cyclic voltammetry (CV), chronoamperometry (CA) and linear sweep voltammetry (LSV). The results suggest that the Ni–B/NPC electrode prepared for 5 min shows the highest electrochemical activity and its redox species coverage and proton diffusion coefficient are remarkably improved compared with the bulk Ni. Ethanol oxidation at the Ni–B/NPC electrode suggests the onset oxidation potential has a negative shift of 52 mV and the oxidation peak current increases by 19.4 times, and apparent activation energy decreases 4.75–30.60 kJ mol<sup>−1</sup> at the same potential, in comparison with the bulk Ni. Additionally, the reaction rate constant for ethanol oxidation at the Ni–B/NPC electrode is improved by about one order of magnitude relative to the reported value. Finally, the Ni–B/NPC electrode has a stable redox behavior after complete activation and superior catalytic stability for ethanol oxidation.

© 2013 Elsevier B.V. All rights reserved.

## 1. Introduction

With the development of fuel cells, there is an urgent need for high-efficient and inexpensive catalysts as substitutes for

expensive noble metal catalysts such as Pt, Au and Pd. The cheap Ni-based catalysts are currently considered as one of the most promising alternative catalytic materials with an excellent electrochemical activity and stability, and their catalytic abilities towards oxidation of alcohols have been studied in alkaline medium since the 1960s–70s [1–3].

Direct methanol fuel cells (DMFCs) as a promising portable mobile power are slowly appearing in public. However, methanol is

\* Corresponding author. Tel.: +86 595 22692512.

E-mail addresses: [yixiongzheng@126.com](mailto:yixiongzheng@126.com), [552199419@qq.com](mailto:552199419@qq.com) (Y.-X. Zheng).

toxic and harmful to the environment [4]. Ethanol considered as a potential alternative fuel has the advantages of nontoxicity, greater availability from the fermentation of biomass and higher theoretical mass energy ( $8 \text{ kWh kg}^{-1}$ ) compared to methanol ( $6 \text{ kWh kg}^{-1}$ ) [4–6]. Many efforts have been devoted to fabricate efficient Ni-based electrocatalysts for ethanol oxidation in alkaline medium.

Nanostructured metal catalysts with high specific surface area often exhibit unique catalytic performance compared to the bulk materials [7]. As a result, different morphologies and structures of nickel-based catalysts have been prepared for ethanol oxidation. For instance, Berchmans et al. [8] modified glassy carbon electrode with nickel oxide; Hayes et al. [9] have prepared Ni–Co mixed oxide on the Pt disk; Liao and co-workers [10] developed Ni/C electrode by electroless technique; Kong et al. [11] showed the nickel nanowire electrode using porous  $\text{Al}_2\text{O}_3$  membrane as a template; Weng et al. [12] fabricated Ni thin film on  $\text{Al}_2\text{O}_3$  substrate; Jin et al. [13] obtained Ni nanoparticles on functional multi-walled carbon nanotubes surfaces by direct electro-deposition; Tian et al. [14] have successfully acquired highly ordered Ni–Cu alloy nanowire arrays by differential pulse current electro-deposition into the pores of a porous anodic  $\text{Al}_2\text{O}_3$  membrane; Zheng et al. [15] studied nano Ni–B amorphous alloy powder microelectrode and electroless Ni–B amorphous alloy microdisk electrode; Stradiotto et al. [16] reported the fabrication of a Ni nanoparticle modified BDD electrode; Hassan et al. [17] used glassy carbon as support for electroless Ni–B coatings electrode; Liu et al. [18] discussed multi-walled carbon nanotube supported Ni catalysts chemically synthesized via a hydrazine reduction process; Muench et al. [7] proposed a template method to synthesize unsupported nickel and nickel–boron tubes. Wang et al. [19] investigated the non-noble catalysts Ni–Co/graphene and Ni/graphene supported on glass carbon electrode.

Among all of them, the nickel-based catalysts could show a good electrocatalytic activity toward ethanol oxidation, however, in such designs, nanoparticles are usually only weakly adsorbed to carbon and  $\text{Al}_2\text{O}_3$  substrate is easily dissolved in alkaline medium. There is a tendency for nanoparticles to agglomerate over time under operating conditions, reducing their active surface area and limiting electrode lifetime [20]. In recent years, nanoporous metals (NPMs) with high specific surface area and high porosity have attracted much attention due to their wide applications in a variety of areas, including selective filtration, chemical sensors, micro-actuators and catalysis [21–23]. Meanwhile, they are regarded as an excellent scaffold material for catalysts in comparison to carbon substrates. Compared with powder sintering method and template method, dealloying method [24] is simple and convenient to prepare three-dimensional bicontinuous NPMs material. The pore and ligament size of the NPMs can be easily tuned by dealloying, varying reaction parameters such as temperature, time. Considering that nanoporous Au and nanoporous Ag are expensive, economic NPC [25,26] has continued to receive considerable interest.

Nickel-based amorphous alloys with the short-range order of atom clusters and long-range disorder structure exhibit an excellent catalytic activity for hydrogenation reaction and hydrogen evolution reaction [27,28], but so far very little work has been studied on the application for fuel cells. In recent years, many efforts have been dedicated toward studying Ni–B amorphous alloy for alcohols oxidation in our previous work [15,29–31]. To the best of our knowledge, the catalytic activity is mainly from nanoscaled surface atoms. In this sense, it is possible to fabricate a highly dispersed Ni–B amorphous surface alloy electrode. In this paper, NPC with high surface area is prepared by chemical dealloying surface Cu–Zn alloy on Cu substrate in acid medium [32]. A novel functional electrocatalyst Ni–B/NPC electrode is prepared by ultrasound-assisted electroless plating, which has the

characteristics of nanoporous materials, the amorphous alloy and surface alloy. Meanwhile, the electrocatalytic activity of the Ni–B/NPC electrode for ethanol oxidation is investigated in alkaline medium.

## 2. Experimental

### 2.1. Preparation of the catalyst

Cu electrodes were prepared with Cu foils ( $4 \text{ mm} \times 5 \text{ mm}$ ) welded on copper wires. Prior to electro-deposition of Zn, the Cu electrodes were polished to a mirror like smoothness with metallographic abrasive paper (1200–3000 grain size), and then in that order put into deionized water with ultrasonic for 10 min, degreasing fluid of  $12 \text{ g L}^{-1}$  NaOH,  $25 \text{ g L}^{-1}$   $\text{Na}_2\text{CO}_3$  and  $60 \text{ g L}^{-1}$   $\text{Na}_3\text{PO}_4 \cdot 12\text{H}_2\text{O}$  for 15 min, deionized water, chemical polishing solution of 60 mL  $\text{H}_3\text{PO}_4$ , 20 mL  $\text{HNO}_3$  and 30 mL HAc for 1.5 min, deionized water and 10 wt.% HCl for 1 min. Then Zn was electrodeposited onto the Cu electrodes at  $20 \text{ mA cm}^{-2}$  for 4 min from Zn plating solution containing  $220 \text{ g L}^{-1}$  KCl,  $62 \text{ g L}^{-1}$   $\text{ZnCl}_2$ ,  $30 \text{ g L}^{-1}$   $\text{H}_3\text{BO}_3$  and 20 mL  $\text{L}^{-1}$  CZ-87 additive (Shanghai Yongsheng Auxiliaries Factory) with the pH of 5–5.6 at 303 K. Where after, the Zn/Cu electrodes were rinsed by deionized water, dried with blower at room temperature and heated at 453 K for 2 h under protection of  $\text{N}_2$  gas. As a result, Cu–Zn alloy was prepared on the surface of Cu electrodes.

NPC samples were fabricated by dealloying of Cu–Zn alloy at 303 K for 60 min in 5 wt.%  $\text{H}_2\text{SO}_4$  solution. After dealloying, these samples were rinsed by deionized water and immersed in deionized water for 1 h to remove residues of  $\text{H}_2\text{SO}_4$  solution. Finally, the samples were dried with blower at room temperature.

The Ni–B/NPC electrode was synthesized by ultrasound-assisted electroless plating method. The composition of the plating bath was  $30 \text{ g L}^{-1}$   $\text{NiCl}_2 \cdot 6\text{H}_2\text{O}$ , 86 mL  $\text{L}^{-1}$  ethylenediamine (EDA),  $1.2 \text{ g L}^{-1}$   $\text{KBH}_4$  and  $40 \text{ g L}^{-1}$  NaOH. The reaction system was placed in a 40 kHz ultrasonic cleaner (Kunshan Ultrasonic Instrument Co., Ltd. KQ3200DE) with ultrasonic power of 40% and operating temperature of 339 K. Different Ni–B/NPC electrodes were prepared as summarized in Table 1. Subsequently, these electrodes were rinsed by deionized water and immersed in deionized water for 1 h to remove residues of plating bath. Finally, the electrodes were dried with blower at room temperature and were used for electro-oxidation measurements. The welded side was covered by insulation glue. All reagents used for the experiment were of analytical grade and the solutions were prepared using deionized water.

The bulk Ni electrode was prepared with the Ni foil ( $4 \text{ mm} \times 5 \text{ mm}$ ) welded on copper wire, and the following treatment was same as the Cu electrodes before electro-deposition of Zn.

### 2.2. Physical characterization

The XRD patterns of the Cu–Zn alloy, NPC and Ni–B/NPC electrodes were recorded using a Bruker (D8 ADVANCE) X-ray diffractometer with Cu  $K_\alpha$  radiation at 40 kV and 40 mA with a scan rate of

**Table 1**  
Preparation of different Ni–B/NPC electrodes.

Electrode sample	Carrier	Reaction condition	Reaction time
Ni–B-3/NPC	NPC	Ultrasonic	3 min
Ni–B-5/NPC	NPC	Ultrasonic	5 min
Ni–B-10/NPC	NPC	Ultrasonic	10 min
Ni–B-15/NPC	NPC	Ultrasonic	15 min
Ni–B-20/NPC	NPC	Ultrasonic	20 min
Ni–B-5/SCF	Smooth Cu foil	Ultrasonic	5 min
Ni–B-5-W/NPC	NPC	Without ultrasonic	5 min

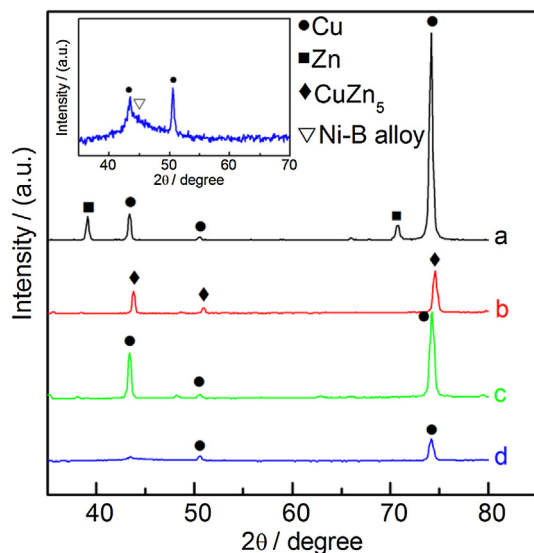


**Fig. 1.** XRD patterns of Cu–Zn samples without thermal treatment (a) and with thermal treatment (b), NPC (c) and Ni–B/NPC amorphous alloy (d). Inset: the magnified curve d.

$6^\circ \text{ min}^{-1}$ ; The morphologies of the electrodes were analyzed by FE-SEM (S-4800, Hitachi).

### 2.3. Electrochemical tests

Electrochemical tests were performed in a conventional three-electrode glass cell at 298 K with a platinum sheet as a counter

electrode, saturated calomel electrode (SCE) as a reference electrode and the Ni–B/NPC electrodes and bulk Ni electrode as a working electrode by using electrochemical workstation (CHI 660D, Shanghai Chenhua instruments, China). The electrolytes consisting of 1 M KOH and different concentrations of ethanol should be free from  $\text{O}_2$  with  $\text{N}_2$  for 15 min. Before electrochemical measurements, the electrodes should be pre-scanned to obtain reproducible curve by CV from 0.05 V to 0.55 V at a scan rate of  $50 \text{ mV s}^{-1}$ .

## 3. Results and discussion

### 3.1. Morphology and structure of the catalyst

**Fig. 1** shows the XRD patterns of the as-prepared Cu–Zn samples before and after thermal treatment, NPC and Ni–B/NPC electrode. As is shown in **Fig. 1**(curve a) after electro-deposition of Zn on the Cu foil, Zn can be well-indexed with the peaks located at  $39.1^\circ$  and  $70.8^\circ$  (JCPDS 04-0831), while the peaks of Cu are located at  $43.4^\circ$ ,  $50.5^\circ$  and  $74.2^\circ$  (JCPDS 04-0836). **Fig. 1**(curve b) exhibits the Cu–Zn sample after thermal treatment at 453 K for 2 h under protection of  $\text{N}_2$ , with the disappearance of Zn and Cu peak, and all the peaks can be assigned to  $\text{CuZn}_5$  alloy (JCPDS 35-1151) as reported in the literature [32], indicating high-temperature heat treatment can be propitious to the interdiffusion of Zn and Cu atoms to form Cu–Zn alloy. It is found that the diffraction peaks of Cu resurface after  $\text{CuZn}_5$  alloy dealloyed in 5%  $\text{H}_2\text{SO}_4$  solution at 303 K for 1 h as illustrated in **Fig. 1**(curve c), suggesting that the Zn is dissolved and NPC is formed. **Fig. 1**(curve d) shows the broad diffraction peak located at around  $45^\circ$  after ultrasound-assisted

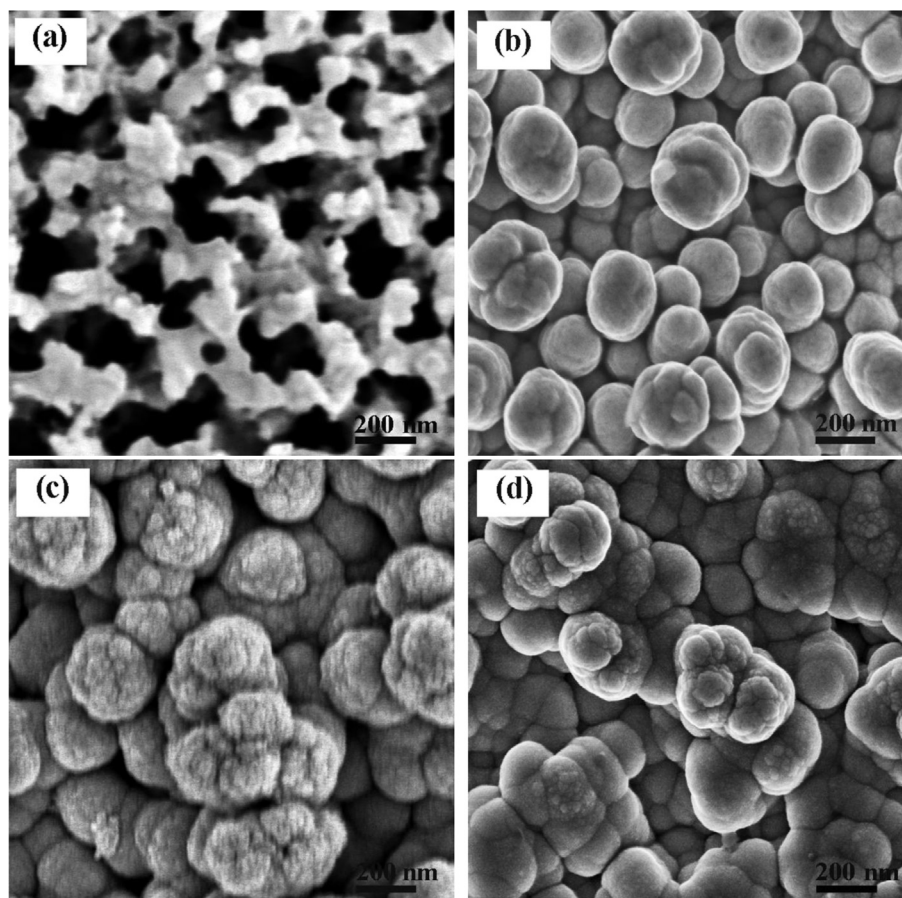


**Fig. 2.** SEM images of the as-prepared NPC (a), Ni–B-5/NPC (b), Ni–B-20/NPC (c) and Ni–B-5-W/NPC (d).



electroless plating on NPC can be ascribed to the diffraction peak of Ni–B alloy [15], manifesting the structure of the Ni–B/NPC alloy is amorphous. However, the diffraction peaks of Cu still appear obviously, elucidating Ni–B/NPC alloy pertains to surface alloy.

Fig. 2 exhibits the SEM images of the as-prepared NPC, Ni–B/NPC electrodes with and without ultrasonic treatment. As is illustrated in Fig. 2a, A rough interconnected NPC with a pore diameter of 100–200 nm and ligament size of 100–200 nm is obtained after CuZn<sub>5</sub> alloy dealloyed in 5% H<sub>2</sub>SO<sub>4</sub> solution at 303 K for 1 h. Fig. 2b shows Ni–B nanoparticles with the size of 150–300 nm are highly dispersed on the NPC after electroless plating with ultrasonic treatment for 5 min. However, the size of Ni–B particles gradually increases with the increase of electroless plating time. From Fig. 2c, as Ni–B alloy is deposited on the NPC after ultrasonic treatment for 20 min, the Ni–B nanoparticles are poorly dispersed and extensive aggregation to form compact structure. In the case of Ni–B-5-W/NPC amorphous alloy (Fig. 2d), the structure is similar to that of the Ni–B-20/NPC amorphous alloy, suggesting that ultrasound plays a role in preventing the agglomeration and improving the dispersity of Ni–B nanoparticles.

### 3.2. Electrochemical performance of the catalyst

Fig. 3 illustrates a comparison of CV curves for the different Ni–B alloy electrodes with the potential range from 0.05 V to 0.55 V in 1 M KOH solution at a scan rate of 50 mV s<sup>−1</sup>. A pair of interesting redox peaks can be observed and should be ascribed to Ni(OH)<sub>2</sub>/NiOOH transformation [15,17] in the anodic and the cathodic directions, respectively. As compared in Fig. 3 (curve a) and Fig. 3 (curve d), the onset oxidation potential and the oxidation peak current density of the Ni–B-5/SCF electrode are estimated as 0.352 V and 6.1 mA cm<sup>−2</sup>, respectively. Meanwhile, the onset oxidation potential and the oxidation peak current density of the Ni–B-5/NPC electrode are estimated as 0.282 V and 124.1 mA cm<sup>−2</sup>, respectively. Obviously, the electrochemical activity of Ni–B-5/SCF electrode is much lower than the Ni–B-5/NPC electrode, indicating that the NPC can enhance the activity of Ni–B electrode. According to Fig. 3 (curve b), the onset oxidation potential and the oxidation

peak current density of the Ni–B-5-W/NPC electrode are 0.302 V and 23.3 mA cm<sup>−2</sup>. Compared with Fig. 3 (curve d), the electrochemical activity of the Ni–B-5/NPC electrode with ultrasonic is significantly higher than that without ultrasonic. The surprising result can be attributed to the good penetrating power and cavitation of ultrasonic, which makes bath fully spread to the surface of NPC and inhibits the agglomeration of Ni–B nanoparticles. The various electroless time of Ni–B electrodes are shown from Fig. 3 (curve c) to Fig. 3 (curve e), notably, as the time increases, the onset oxidation potential presents a slight increase and the oxidation peak current densities have a dramatic increase, finding that Ni–B-5/NPC electrode has the highest electrochemical activity. This is due to the Ni–B nanoparticles highly dispersed on the NPC after electroless plating with ultrasonic for 5 min. Then the dispersion of Ni–B nanoparticles gradually weakens with the further increase of electroless plating time. This result is consistent with Fig. 2b and c. As a result, Ni–B-5/NPC electrode is used in the following electrochemical measurements.

Fig. 4A and B present CV curves of the Ni–B-5/NPC and bulk Ni electrodes in 1 M KOH solution at different scan rates from 10 to 100 mV s<sup>−1</sup>. As is shown in the figures, the values of the anodic and the cathodic peak currents increase with the increasing of scan rate, additionally, the anodic peak potential has a positive shift towards more positive values and the cathodic peak potential displays a negative shift towards more negative values.

The variation of the anodic and the cathodic peak currents with the scan rate for the Ni–B-5/NPC and bulk Ni electrodes is exhibited in Fig. 4C and D. According to linear fitting, the peak current values of Ni(OH)<sub>2</sub>/NiOOH redox couple are linearly proportional to the scan rate, and the surface coverage of Ni(OH)<sub>2</sub>/NiOOH redox species of the Ni–B-5/NPC and bulk Ni electrodes can be obtained from the following equation [33]:

$$I_p = \left( \frac{n^2 F^2}{4RT} \right) \nu A \Gamma^* \quad (1)$$

where  $I_p$ ,  $n$ ,  $A$ ,  $\nu$  and  $\Gamma^*$  are the peak current, the number of transferred electron, apparent area of the electrode, the potential scan rate and the surface coverage of the redox species, respectively.  $\Gamma^*$  values of the Ni–B-5/NPC and bulk Ni electrodes are separately calculated to be  $1.62 \times 10^{-6}$  mol cm<sup>−2</sup> and  $6.04 \times 10^{-8}$  mol cm<sup>−2</sup> deriving from the average of the anodic and the cathodic results. It is obvious that the Ni–B-5/NPC electrode has a significantly high oxidation peak current attributing to the larger surface coverage of redox species, and the  $\Gamma^*$  value is higher about one order of magnitude than that calculated at the Ni–B/C ( $1.25 \times 10^{-7}$  mol cm<sup>−2</sup>) electrode [17].

Fig. 4E and F show a good linear dependence of the anodic and the cathodic peak current of the Ni–B-5/NPC and bulk Ni electrodes on the square root of the scan rate according to the data fitting, implying the total redox transition of Ni(OH)<sub>2</sub> is diffusion controlled process, consistent with other reported in papers [17,19]. As is reported in the literature [34–36], the electrochemical reaction of the surface Ni(OH)<sub>2</sub> of the nickel electrode is controlled by the solid phase body of the proton diffusion, and therefore the proton diffusion coefficient has been an important parameter for characterization of the electrochemical performance of nickel electrodes. The proton diffusion coefficient can be calculated using the following equation [37] in 298 K:

$$I_p = 2.65 \times 10^5 n^{3/2} A D^{1/2} C \nu^{1/2} \quad (2)$$

where  $I_p$ ,  $n$ ,  $A$ ,  $D$  and  $C$  are the anodic peak current, the number of transferred electron, apparent area of the electrode, the proton diffusion coefficient and the proton concentration, respectively. The

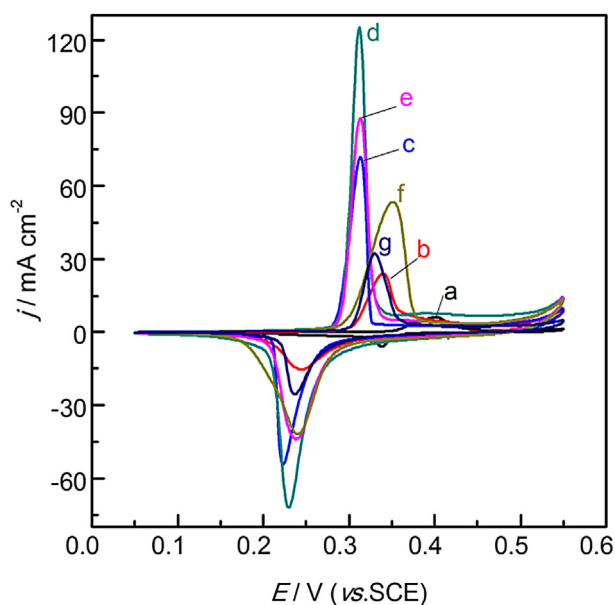
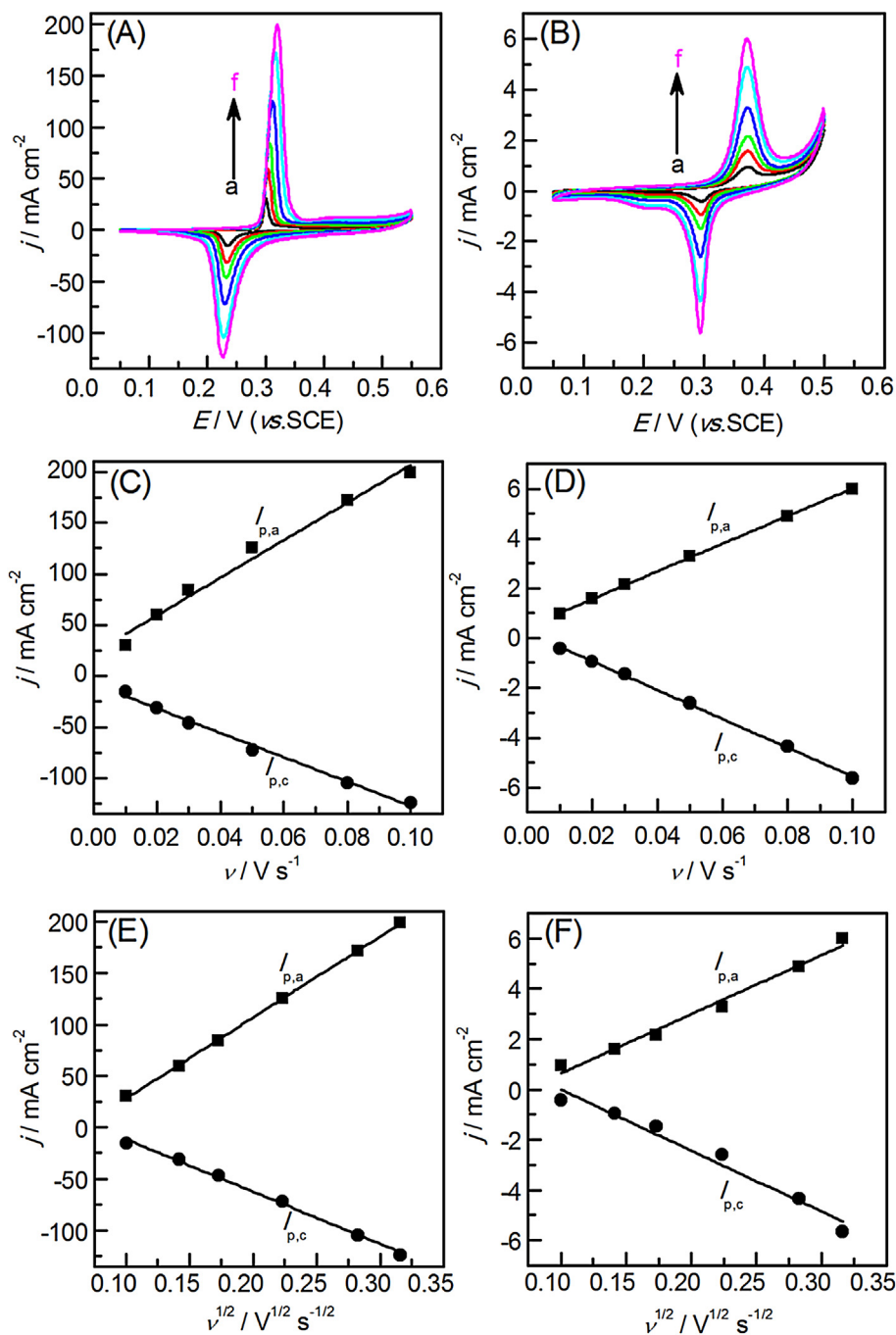


Fig. 3. CV curves of Ni–B-5/SCF (a), Ni–B-5-W/NPC (b), Ni–B-3/NPC (c), Ni–B-5/NPC (d), Ni–B-10/NPC (e), Ni–B-15/NPC (f) and Ni–B-20/NPC (g) electrodes in 1 M KOH solution at a scan rate of 50 mV s<sup>−1</sup>.



**Fig. 4.** CV curves of the Ni-B-5/NPC (A) and bulk Ni electrodes (B) in 1 M KOH solution at different scan rates, a: 10, b: 20, c: 30, d: 50, e: 80 and f: 100  $\text{mV s}^{-1}$ . The variation of the anodic and the cathodic peak currents with the scan rate for the Ni-B-5/NPC (C) and bulk Ni electrodes (D) and the dependence of the anodic and the cathodic peak currents on the square root of the scan rate for the Ni-B-5/NPC (E) and bulk Ni electrodes (F).

proton concentration in the nickel hydroxide is assumed to be the same as that of  $\text{Ni}(\text{OH})_2$  from the stoichiometry of reaction from the following reaction [37]:



The concentration of  $\text{Ni}(\text{OH})_2$  is estimated as  $3.97 \text{ g cm}^{-3}$  [38]. The values of proton diffusion coefficient are calculated to be around  $4.81 \times 10^{-9}$  and  $4.27 \times 10^{-12} \text{ cm}^2 \text{ s}^{-1}$  for Ni-B-5/NPC and bulk Ni electrodes, respectively. As is shown in Fig. 4A and B, the onset oxidation potential of the Ni-B-5/NPC electrode is more

negative than that of the bulk Ni electrode at the same scan rate, ascribed to the much larger proton diffusion coefficient.

The roughness of the electrode can intuitively reflect its real surface area and can be conveniently obtained by CA. Fig. 5 suggests a comparison of chronoamperograms for different electrodes in 1 M KOH solution with step potential from 100 mV to 110 mV. The electric double layer differential capacitance is calculated by differential capacitance technique [39] according to the following equations:

$$C_d = dq/dE = idt/dE \quad (4)$$

Here,  $C_d$  is electric double layer differential capacitance. Then compared the  $C_d$  value of electrode with the  $C_d$  value of the pure mercury electrode ( $20 \mu\text{F cm}^{-2}$ ), the real surface area of the bulk Ni electrode, Ni–B-5-W/NPC electrode, Ni–B-5/NPC electrode and Ni–B-20/NPC electrode can be respectively estimated as  $3.9 \text{ cm}^2$ ,  $8.1 \text{ cm}^2$ ,  $42.8 \text{ cm}^2$  and  $9.5 \text{ cm}^2$ , corresponding to their roughness calculated to be 20, 41, 214 and 48 according to the real surface area of electrode divided by the apparent area. Obviously, the Ni–B-5/NPC electrode has the largest roughness, and the roughness of the Ni–B-20/NPC and Ni–B-5-W/NPC electrode is almost close. As previously mentioned, the Ni–B-5/NPC electrode has a larger proton diffusion coefficient and more negative onset oxidation potential. This behavior can be attributed to the dispersion of Ni–B nanoparticles with a high real surface area, which can enhance the contact of the electrode surface with the electrolyte and shorten the diffusion distance of proton in the  $\text{Ni}(\text{OH})_2$  solid phase to increase the proton conductivity.

### 3.3. Electrocatalytic activity of the catalyst for ethanol oxidation

Fig. 6A displays CV curves of the Ni–B-5/NPC electrode in 1 M KOH solution in presence of different concentrations of ethanol at the scan rate of  $10 \text{ mV s}^{-1}$ . It is clearly observed that the oxidation peak current density increases a lot in presence of 0.05 M ethanol contrasting sharply with the absence of ethanol in 1 M KOH solution and augments with the increasing concentration of ethanol, and the oxidation peak potential is around 0.4 V. This is due to  $\text{Ni}(\text{OH})_2$  transformed into  $\text{NiOOH}$  considered as a strong oxidant in the anodic direction.  $\text{NiOOH}$  can be used for the oxidation of adsorbed ethanol molecules on the electrode surface and can be reduced to  $\text{Ni}(\text{OH})_2$  at the same time. The higher the concentration of ethanol is present, the more reduction of  $\text{NiOOH}$  back to  $\text{Ni}(\text{OH})_2$  is and the greater oxidation peak current density of  $\text{Ni}(\text{OH})_2$  appears, indicating ethanol molecules adsorbed on the electrode surface are oxidized at higher potentials parallel to the oxidation of  $\text{Ni}(\text{OH})_2$  to  $\text{NiOOH}$ . Intriguingly, the anodic current passes through a maximum and then drops a little as the potential is anodically swept. This may be ascribed to the effect of products or intermediates adsorbed on the electrode surface with the consequence of decreasing the number of sites for ethanol adsorption. In

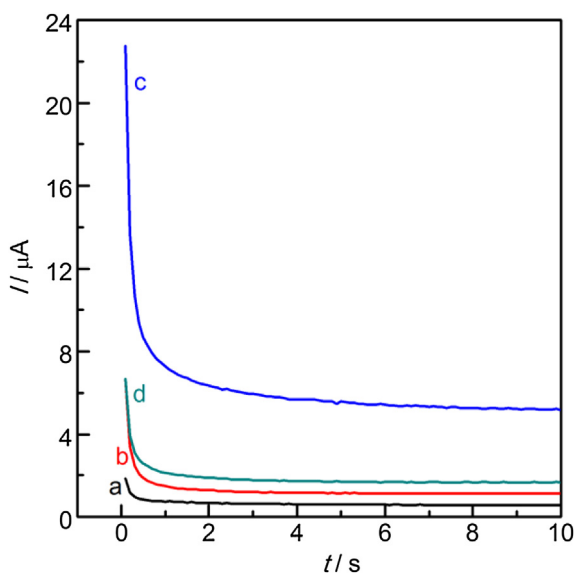


Fig. 5. Chronoamperograms of the bulk Ni (a), Ni–B-5-W/NPC (b), Ni–B-5/NPC (c) and Ni–B-20/NPC (d) electrodes in 1 M KOH solution, step potential from 100 mV to 110 mV.

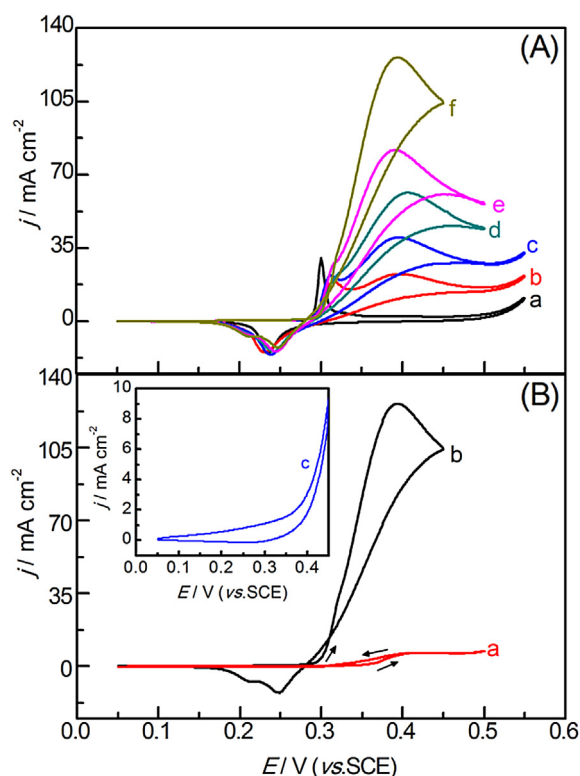
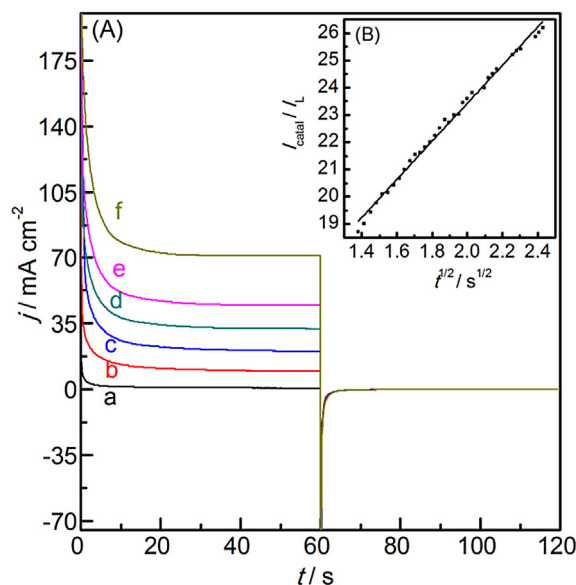


Fig. 6. (A) CV curves of the Ni–B-5/NPC electrode in 1 M KOH solution in presence of different concentrations of ethanol, a: 0, b: 0.05, c: 0.1, d: 0.15, e: 0.2 and f: 0.3 M. (B) CV curves for different electrodes in 1 M KOH solution in presence of 0.3 M ethanol, a: bulk Ni, b: Ni–B-5/NPC, c: NPC (inset). Scan rate =  $10 \text{ mV s}^{-1}$ .

addition, the electrocatalytic oxidation of ethanol occurs not only in the anodic direction but also in the initial stage of the cathodic direction. It is found that current density increases with the increasing concentration of ethanol in the initial stage of the cathodic half cycle, suggesting that the surface of ethanol and its oxidation intermediates could not be completely oxidized in the anodic scan and continue to be oxidized at the high potential in the cathodic scan. The intersecting CV curve in presence of 0.3 M ethanol can support the opinion.

Fig. 6B illustrates CV curves for the bulk Ni, Ni–B-5/NPC and NPC (inset) electrodes in 1 M KOH solution in presence of 0.3 M ethanol at the scan rate of  $10 \text{ mV s}^{-1}$ . A small current is observed from the NPC electrode. As illustrated in the figure, the onset oxidation potential is estimated as 0.348 and 0.296 V for the bulk Ni and Ni–B-5/NPC electrodes. Meanwhile, the oxidation peak current density of ethanol oxidation is 6.5 and  $126.2 \text{ mA cm}^{-2}$  for the bulk Ni and Ni–B-5/NPC electrodes. Apparently, the Ni–B-5/NPC electrode shows a higher electrocatalytic activity for ethanol oxidation. To some extent, this may be due to the high surface area of the electrode conducive to the mass transfer process and ethanol adsorption, accelerating ethanol oxidation and greatly improving the catalytic activity of the electrode.

Double potential step CA method is a convenient technique to determine the electrocatalytic oxidation rate constant of active materials at the electrode. To measure the catalytic rate constant of ethanol oxidation at the Ni–B-5/NPC electrode, double potential step chronoamperograms in 1 M KOH solution with different concentrations of ethanol are recorded in Fig. 7A by setting the potential steps at 450 mV (first step) and 100 mV (second step). The current response increases dramatically with the increasing concentration of ethanol at the first potential step and tends to be



**Fig. 7.** (A) Double potential step chronoamperograms of the Ni-B-5/NPC electrode in 1 M KOH solution with different concentrations of ethanol, a: 0, b: 0.05, c: 0.1, d: 0.15, e: 0.2 and f: 0.3 M. Potential steps are 450 mV and 100 mV. Inset (B) Dependence of  $I_{\text{cat}}/I_L$  on  $t^{1/2}$  derived from the data of double potential step chronoamperograms of 0.15 M ethanol and in absence of ethanol.

stable quickly, indicating that the Ni-B-5/NPC electrode has an excellent and stable electrocatalytic activity for ethanol oxidation. The mechanism of electrocatalytic reaction by CA has been proposed for determination of the reaction rate constant [40]. According to the equation:

$$I_{\text{cat}}/I_L = \lambda^{0.5} [\pi^{0.5} \text{erf}(\lambda^{0.5}) + \exp(-\lambda)/\lambda^{0.5}] \quad (5)$$

where  $I_{\text{cat}}$  and  $I_L$  are the currents of the Ni-B-5/NPC electrode in the presence and absence of ethanol, respectively,  $\lambda = kCt$  is the argument of the error function,  $k$  is the catalytic reaction rate constant,  $C$  is the concentration of ethanol and  $t$  is the elapsed time. If  $\lambda > 1.5$ ,  $\text{erf}(\lambda^{0.5}) \rightarrow 1$ ,  $\exp(-\lambda)/\lambda^{0.5} \rightarrow 0$ , the Equation (5) is reduced to:

$$I_{\text{cat}}/I_L = \lambda^{0.5} \pi^{0.5} = \pi^{0.5} (kCt)^{0.5} \quad (6)$$

The plot of  $I_{\text{cat}}/I_L$  vs  $t^{1/2}$  derived from the data of chronoamperograms in presence of 0.15 M ethanol and in absence of ethanol in 1 M KOH solution at the Ni-B-5/NPC electrode is exhibited in Fig. 7B. According to Equation (6) and the slope of  $I_{\text{cat}}/I_L$  against  $t^{1/2}$ , the value of the reaction rate constant is obtained as  $1.03 \times 10^5 \text{ cm}^3 \text{ mol}^{-1} \text{ s}^{-1}$ . It is improved by about one order of magnitude in comparison with the reported value on the nickel modified NiOOH electrode ( $9.64 \times 10^3 \text{ cm}^3 \text{ mol}^{-1} \text{ s}^{-1}$ ) [41].

In many of the temperature-dependent alcohols oxidation studies, the calculations of the apparent activation energy of them at the electrode are of great significance. The apparent activation energy can be determined by LSV. Fig. 8 presents LSV curves of the Ni-B-5/NPC (inset in figure A) and bulk Ni (inset in figure B) electrodes carried out at 5 K intervals from 283 to 313 K in 1 M KOH solution containing 0.3 M ethanol at a scan rate of  $5 \text{ mV s}^{-1}$  with the potential range from 0.2 to 0.45 V. As shown in the insert figure, the peak current density augments significantly with the increase of temperature and the onset oxidation potential has a negative shift at the Ni-B-5/NPC and bulk Ni electrodes, indicating that the electrocatalytic activity for ethanol oxidation is improved. The oxidation peaks shown in the LSV are ascribed to the transform of

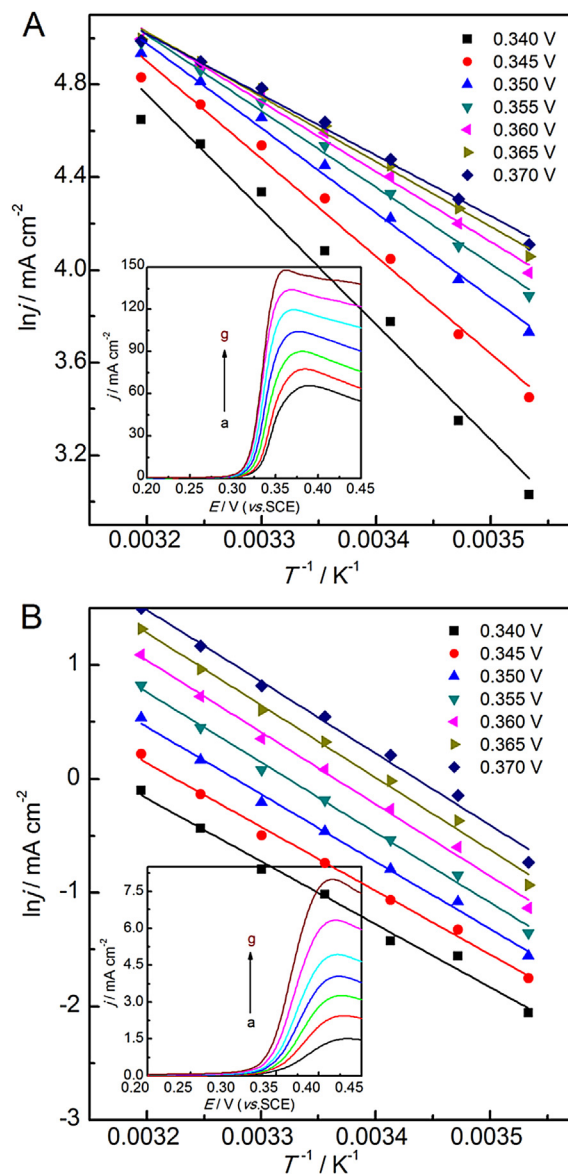


**Fig. 8.** LSV curves of the Ni-B-5/NPC (inset in figure A) and bulk Ni (inset in figure B) electrodes in 1 M KOH solution containing 0.3 M ethanol with different temperatures at a scan rate of  $5 \text{ mV s}^{-1}$ , a: 283, b: 288, c: 293, d: 298, e: 303, f: 308 and g: 313 K. Arrhenius plots for the Ni-B-5/NPC (A) and bulk Ni (B) electrodes in 1 M KOH solution containing 0.3 M ethanol at different potentials.

surface oxides parallel to ethanol oxidation. The values of the apparent activation energy for ethanol oxidation are obtained according to the equation [42]:

$$j = A \exp(-E_a/RT) \quad (7)$$

$$\ln j = \ln A - E_a/RT \quad (8)$$

Here,  $j$  is the current density at a specific potential,  $R$  is the gas constant,  $T$  is the temperature, and  $E_a$  is the apparent activation energy at a specific potential. Arrhenius plots of the Ni-B-5/NPC and bulk Ni electrodes for 0.3 M ethanol at different potentials derived from the data of LSV curves are shown in Fig. 8A and B. According to linear fitting for  $\lg j$  against  $1/T$ , the values of  $E_a$  at different potential are summarized in Table 2. Obviously, the  $E_a$  for ethanol oxidation at the Ni-B-5/NPC electrode is lower than that at



**Table 2**

$E_a$  for the Ni–B-5/NPC and bulk Ni electrodes in 1 M KOH solution containing 0.3 M ethanol.

$E^a$ [V]	$E_a$ value of Ni–B-5/NPC [kJ mol <sup>−1</sup> ]	$E_a$ value of bulk Ni [kJ mol <sup>−1</sup> ]
0.340	41.25	46.00
0.345	34.97	46.63
0.350	30.34	49.24
0.355	27.34	51.24
0.360	25.06	52.48
0.365	23.23	52.85
0.370	21.75	52.35

<sup>a</sup> The applied potential.

the bulk Ni electrode under the same potential, and this further explains the better electrocatalytic activity of the Ni–B-5/NPC electrode for ethanol oxidation. Interestingly, the  $E_a$  for ethanol oxidation at the Ni–B-5/NPC electrode decreases with the increasing of potential, manifesting that ethanol is more easily oxidized at a higher potential.

### 3.4. Stability of the catalyst

Stability is one of the most important parameters of electrocatalyst. CV is a traditional method used for determination of the stability of electrocatalyst. Fig. 9A and B show CV curves of the Ni–B-5/NPC electrode at different scan cycles in 1 M KOH solution at a scan rate of 50 mV s<sup>−1</sup> and Fig. 9C shows the variation of the anodic oxidation peak current with cycling number for the Ni–B-5/NPC electrode. As is shown in the figure, the anodic oxidation peak current increases with the increasing number of potential cycles and the onset oxidation potential has almost no change, indicating that the thickness of nickel oxide layer gradually increases and the electrode is in the activation stage. Then the oxidation peak current reaches the highest, suggesting that the Ni–B-5/NPC electrode has complete activation and exhibits stable redox behavior of the

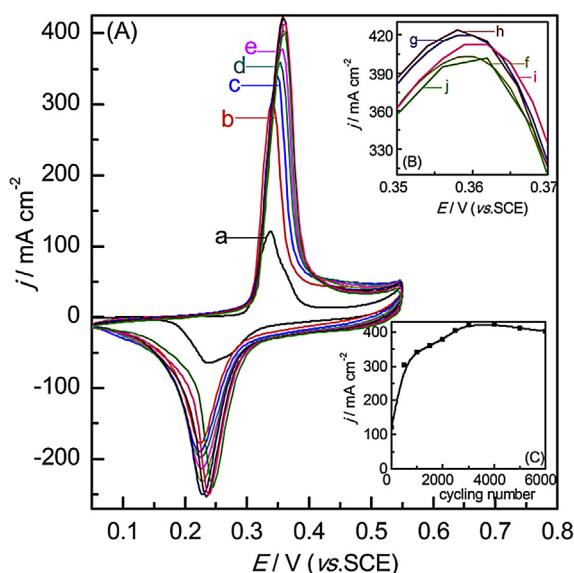


**Fig. 9.** (A) CV curves of the Ni–B-5/NPC electrode at different cycling number in 1 M KOH solution at a scan rate of 50 mV s<sup>−1</sup>, a: 1<sup>st</sup>, b: 500<sup>th</sup>, c: 1000<sup>th</sup>, d: 1500<sup>th</sup>, e: 2000<sup>th</sup>, f: 2500<sup>th</sup>, g: 3000<sup>th</sup>, h: 4000<sup>th</sup>, i: 5000<sup>th</sup> and j: 6000<sup>th</sup> cycle. Inset (B) The magnified curves from f to j. Inset (C) The variation of the anodic oxidation peak current with cycling number for the Ni–B-5/NPC electrode.

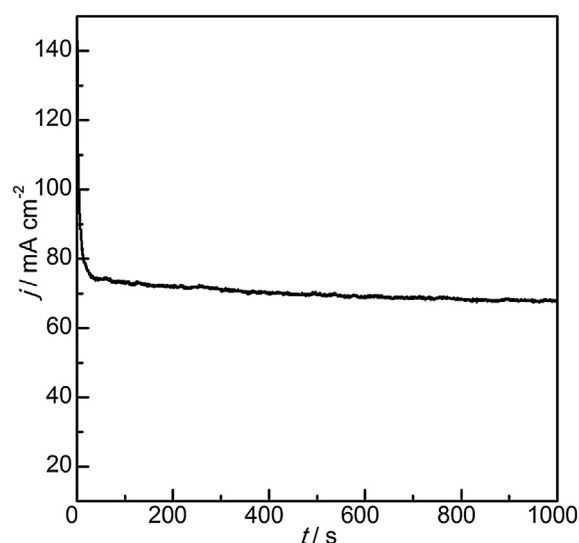


**Fig. 10.** Chronoamperogram of the Ni–B-5/NPC electrode in the presence of 0.3 M ethanol in 1 M KOH solution at a potential step of 0.5 V for 1000 s.

NiOOH/Ni(OH)<sub>2</sub> couple between 3000 and 4000 potential cycles. After 4000 potential cycles, the oxidation peak current decreases with the increasing number of potential cycles, decreasing to 94.8% with respect to oxidation peak current of the 3000<sup>th</sup> cycle after 6000 potential cycles. This is due to the activity loss of the nickel oxide [43].

CA is also used to further evaluate the activity and stability of the Ni–B-5/NPC electrode for ethanol oxidation. Fig. 10 depicts the chronoamperogram of the Ni–B-5/NPC electrode in the presence of 0.3 M ethanol in 1 M KOH solution at a potential step of 0.5 V for 1000 s. As displayed in the figure, the initial current is dropped sharply in the first 200 s, and then followed by a slower decrease over time. This is pertinent to the adsorption of intermediate species during the initial stage, blocking some active sites of ethanol oxidation. Although the current gradually decreases after long-time operation, it is obvious that the attenuation of the current is relatively slow, suggesting the Ni–B-5/NPC electrode has a good stability toward ethanol oxidation.

## 4. Conclusion

In summary, a novel nanostructured Ni–B/NPC amorphous alloy electrode is successfully fabricated by combining the dealloying method and ultrasonic-assisted electrodeless technique. In contrast, the Ni–B/NPC prepared for 5 min shows the highest electrochemical activity among the other Ni–B/NPC electrodes. Intriguingly, the values of  $D$  and  $\Gamma^*$  at the Ni–B/NPC electrode are three orders and one order of magnitude as large as the bulk Ni electrode, respectively, and the result of ethanol oxidation in KOH solution suggests that the onset oxidation potential has a negative shift of 52 mV and the oxidation peak current density increases by 19.4 times in comparison with the bulk Ni electrode. Meanwhile, it is found that the reaction rate constant ( $k$ ) for ethanol oxidation at the Ni–B/NPC electrode is improved by about one order of magnitude compared with the reported value. Additionally, the activation energy and long-term stability for ethanol oxidation are investigated. The enhanced electrocatalytic activity and stability for ethanol oxidation at the Ni–B/NPC electrode may be ascribed to the high surface area conducive to the mass transfer process and ethanol adsorption and the structural effect of NPC and Ni–B amorphous alloy nanoparticles. This study may promote new amorphous functional nanomaterials development for fuel cells.



## Acknowledgments

This work is supported by the Fujian Provincial Natural Science Foundation (No. 2010J01292), the Fund of Fujian Provincial Key Laboratory of Nanomaterials (No. NM10-04) and the Program for Excellent Talents of Huaqiao University, PR China (No. 08BS205).

## References

- [1] K. Nakagawa, R. Konaka, T. Nakata, *J. Org. Chem.* 27 (1962) 1597–1601.
- [2] M. Fleischmann, K. Korinek, D. Pletcher, *J. Electroanal. Chem. Interfacial Electrochem.* 31 (1971) 39–49.
- [3] M. Amjad, D. Pletcher, C. Smith, *J. Electrochem. Soc.* 124 (1977) 203–206.
- [4] E. Antolini, *J. Power Sources* 170 (2007) 1–12.
- [5] S.C.S. Lai, M.T.M. Koper, *Phys. Chem. Chem. Phys.* 11 (2009) 10446–10456.
- [6] Y.Y. Huang, J.D. Cai, M.Y. Liu, Y.L. Guo, *Electrochim. Acta* 83 (2012) 1–6.
- [7] F. Muench, M. Oezaslan, M. Rauber, S. Kaserer, A. Fuchs, E. Mankel, J. Brötz, P. Strasser, C. Roth, W. Ensinger, *J. Power Sources* 222 (2013) 243–252.
- [8] S. Berchmans, H. Gomathi, G. Prabhakara Rao, *J. Electroanal. Chem.* 394 (1995) 267–270.
- [9] E.T. Hayes, B.K. Bellingham, H.B. Mark, J.A. Galal, *Electrochim. Acta* 41 (1996) 337–344.
- [10] Y.Y. Liao, T.C. Chou, *Electroanalysis* 12 (2000) 55–59.
- [11] J.L. Kong, K.H. Xue, Y. Shao, C.J. He, Q.L. Chen, *Acta Phys. Chim. Sin.* 18 (2002) 268–271.
- [12] Y.C. Weng, J.F. Rick, T.C. Chou, *Biosens. Bioelectron.* 20 (2004) 41–51.
- [13] G.P. Jin, Y.F. Ding, P.P. Zheng, *J. Power Sources* 166 (2007) 80–86.
- [14] X.K. Tian, X.Y. Zhao, L.D. Zhang, C. Yang, Z.B. Pi, S.X. Zhang, *Nanotechnology* 19 (2008) 1–6.
- [15] Y.X. Zheng, S.B. Yao, S.M. Zhou, *Acta Phys. Chim. Sin.* 24 (2008) 1643–1649.
- [16] N.R. Stradiotto, K.E. Toghill, L. Xiao, A. Moshar, R.G. Compton, *Electroanalysis* 21 (2009) 2627–2633.
- [17] H.B. Hassan, Z. Abdel Hamid, *Int. J. Hydrogen Energy* 36 (2011) 849–856.
- [18] Z. Liu, Z.L. Li, F. Wang, J.J. Liu, J. Ji, J.J. Wang, W.H. Wang, S.Y. Qin, L.H. Zhang, *Mater. Lett.* 65 (2011) 3396–3398.
- [19] Z.H. Wang, Y.L. Du, F.Y. Zhang, Z.X. Zheng, Y.Z. Zhang, C.M. Wang, *J. Solid State Electrochem.* 17 (2013) 99–107.
- [20] Y. Ding, M.W. Chen, J. Erlebacher, *J. Am. Chem. Soc.* 126 (2004) 6876–6877.
- [21] P.P. Liu, X.B. Ge, R.Y. Wang, H.Y. Ma, Y. Ding, *Langmuir* 25 (2009) 561–567.
- [22] C.X. Xu, Y.Q. Liu, F. Su, A.H. Liu, H.J. Qiu, *Biosens. Bioelectron.* 27 (2011) 160–166.
- [23] J. Cai, J. Xu, J.M. Wang, L.Y. Zhang, H. Zhou, Y. Zhong, D. Chen, H.Q. Fan, H.B. Shao, J.Q. Zhang, C.N. Cao, *Int. J. Hydrogen Energy* 38 (2013) 934–941.
- [24] J. Erlebacher, M.J. Aziz, A. Karma, N. Dimitrov, K. Sieradzki, *Nature* 410 (2001) 450–459.
- [25] D.Q. Liu, Z.B. Yang, P. Wang, F. Li, D.S. Wang, D.Y. He, *Nanoscale* 5 (2013) 1917–1921.
- [26] F.L. Jia, J.H. Zhao, X.X. Yu, *J. Power Sources* 222 (2013) 135–139.
- [27] Q. Han, K.R. Liu, J.S. Chen, X. Li, X.J. Wei, *Int. J. Hydrogen Energy* 29 (2004) 243–248.
- [28] G.Y. Bai, Z. Zhao, L.B. Niu, H.X. Dong, M.D. Qiu, F. Li, Q.Z. Chen, G.F. Chen, *Catal. Commun.* 23 (2012) 34–38.
- [29] Y.X. Zheng, S.B. Yao, S.M. Zhou, *Acta Phys. Chim. Sin.* 20 (2004) 1352–1356.
- [30] Y.X. Zheng, S.B. Yao, S.M. Zhou, *Electrochemistry* 13 (2007) 307–311.
- [31] Y.X. Zheng, J. Huaqiao Univ. Nat. Sci. 31 (2010) 422–425.
- [32] F.L. Jia, C.F. Yu, K.J. Deng, L.Z. Zhang, *J. Phys. Chem. C* 111 (2007) 8424–8431.
- [33] A.J. Bard, L.R. Faulkner, *Electrochemical Methods, Fundamentals and Applications* (Y.H. Shao, G.Y. Zhu, X.D. Dong, B.L. Zhang Trans.), second ed., Chemical Industry Press, Beijing, 2005, p. 409.
- [34] D.M. Mac Arthur, *J. Electrochem. Soc.* 117 (1970) 422–426.
- [35] C.J. Zhang, S.M. Park, *J. Electrochem. Soc.* 134 (1987) 2966–2970.
- [36] J.L. Kong, K.H. Xue, C.J. He, Y. Shao, Q.L. Chen, J.L. Yao, Y. Xie, Z.Q. Tian, *Chin. J. Appl. Chem.* 18 (2001) 462–465.
- [37] X.Y. Wang, J. Yan, Y.S. Zhang, H.T. Yuan, D.Y. Song, *J. Appl. Electrochem.* 28 (1998) 1377–1382.
- [38] M. Oshitani, T. Takayama, K. Takashima, S. Tsuji, *J. Appl. Electrochem.* 16 (1986) 403–412.
- [39] Y.D. Shu, B.Z. Chen, *Metallurge Electrochem of Studying Methods*, Central South University of Technology Press, Changsha, 1990, p. 177.
- [40] A.J. Bard, L.R. Faulkner, *Electrochemical Methods, Fundamentals and Applications* (Y.H. Shao, G.Y. Zhu, X.D. Dong, B.L. Zhang Trans.), second ed., Chemical Industry Press, Beijing, 2005, pp. 329–352.
- [41] I. Danaee, M. Jafarian, M. Sharafi, F. Gopal, *J. Electrochem. Sci. Technol.* 3 (2012) 50–56.
- [42] J.L. Cohen, D.J. Volpe, H.D. Abruna, *Phys. Chem. Chem. Phys.* 9 (2007) 49–77.
- [43] R.M. Abdel Hameed, K.M. El-Khatib, *Int. J. Hydrogen Energy* 35 (2010) 2517–2529.